

# High Resolution Imaging of a Black Hole Shadow with Millimetron Orbit around Lagrange Point L2

S. F. Likhachev<sup>1</sup>, A. G. Rudnitskiy<sup>1\*</sup>, M. A. Shchurov<sup>1</sup>, A. S. Andrianov<sup>1</sup>, A. M. Baryshev<sup>2</sup>,  
S. V. Chernov<sup>1</sup>, V. I. Kostenko<sup>1</sup>

<sup>1</sup>*Astro Space Center, Lebedev Physical Institute, Russian Academy of Sciences, Profsoyuznaya str. 84/32, Moscow, 117997, Russia*

<sup>2</sup>*Kapteyn Astronomical Institute, University of Groningen, P.O. Box 800, 9700 AV Groningen, the Netherlands*

Accepted XXX. Received YYY; in original form ZZZ

## ABSTRACT

Imaging of the shadow around supermassive black hole (SMBH) horizon with a very long baseline interferometry (VLBI) is recognized recently as a powerful tool for experimental testing of Einstein’s General relativity. The Event Horizon Telescope (EHT) has demonstrated that an Earth-extended VLBI with the maximum long base ( $D = 10,700$  km) can provide a sufficient angular resolution  $\theta \sim 20 \mu\text{as}$  at  $\lambda = 1.3$  mm ( $\nu = 230$  GHz) for imaging the shadow around SMBH located in the galaxy M87. However, the accuracy of critically important characteristics, such as the asymmetry of the crescent-shaped bright structure around the shadow and the sharpness of a transition zone between the shadow floor and the bright crescent silhouette, both of order  $\Delta\theta \sim 4 \mu\text{as}$ , is still to be improved. In our previous paper we have shown that Space-Earth VLBI observation within a joint Millimetron and EHT configuration at the near-Earth high elliptical orbit (HEO) can considerably improve the image quality. Even more solid grounds for firm experimental validation of General relativity can be obtained with a higher resolution available within the joint Millimetron and EHT program at the Lagrangian point L2 in the Sun-Earth system with an expected resolution of  $\Delta\theta \sim 0.1 \mu\text{m}$ . In this paper we argue that in spite of limitations of L2 orbit an adequate sparse ( $u, v$ ) coverage can be achieved and the imaging of the shadows around Sgr A\* and M87\* can be performed with a reasonable quality.

**Key words:** instrumentation: high angular resolution – instrumentation: interferometers – quasars: supermassive black holes

## 1 INTRODUCTION

Observations of supermassive black holes (SMBH) in far-infrared (FIR) and sub-millimeter wavebands with high angular resolution provide a unique opportunity to test the Einstein’s theory of General relativity (GR, see discussion in Cunha & Herdeiro 2018; Event Horizon Telescope Collaboration et al. 2019a; Psaltis 2019; Berti 2019, and references therein). Direct observations of SMBH – the objects that by definition are unseen, are possible through imaging of a bright crescent-like ring bordering the shadow around the black hole event horizon. In case of a spherically symmetric black hole the shadow radius is  $r_s \approx 5r_S$  with  $r_S = 2GM/c^2$  being the radius of Schwarzschild (horizon) surface. The shadow shape is determined by physical characteristics of the SMBH itself (its mass  $M$  and spin  $a$ ) and by the angle between the black hole spin and the observer line of sight. Bright light in the crescent is collected from the entire disc flow accreting on to the SMBH, and as such manifests physical characteristic of the inflow. Therefore, observations of the SMBH shadow and brightness distribution in the crescent provide the full information not only to quantify the space-time geometry around it, but to understand physics of processes in plasma in such strong gravitational fields as well.

The Event Horizon Telescope collaboration (EHT) was the first to scrutinize and confirm experimentally this understanding. Suc-

cessful imaging of the SMBH in the centre of the galaxy M87\* has demonstrated also that firm ultimate conclusion and quantitative characterization urges a much higher angular resolution with interferometric baselines longer than Earth diameter. The maximum angular resolution reached by EHT  $\Delta\theta \sim 20 \mu\text{as}$  at  $\lambda = 1.3$  mm, i.e. a half of the angular size of the M87\* SMBH  $\Delta\theta \sim 40 \mu\text{as}$  being at the edge of the diffraction limit. Therefore, either Space-Earth or Space-Space VLBI program (S-E VLBI or S-S VLBI, correspondingly) are needed to advance direct experimental examination of General relativity (see discussions in Roelofs et al. 2019; Andrianov et al. 2021; Novikov et al. 2021).

In our recent paper (Andrianov et al. 2021) it was shown that a S-E VLBI experiment with a high elliptical orbit around Earth can provide a better image quality of both Sgr A\* and M87\* nearby SMBH even in an image dynamical mode, with a higher fidelity and a better nearly proportional to the angular resolution asymmetry test. From this point of view, this is achieved despite of a sparse ( $u, v$ ) coverage typical for single space based station of S-E VLBI. It seems reasonable to expect that result for experiments with an even higher angular resolution ( $\Delta\theta \sim 0.1 \mu\text{as}$ ) at the Sun-Earth Lagrangian libration point L2 (for details see Section 2). On the other hand though, a common view is that a ( $u, v$ ) coverage with baselines at L2 and a group of available ground-based stations would be insufficient for imaging with reasonable quality.

Our current paper aims to demonstrate that this is not exactly the case. In fact ( $u, v$ ) coverage which is very similar to Earth VLBI can

\* E-mail: arud@asc.rssi.ru

**Table 1.** Parameters of VLBI Mode of Millimetron Space Observatory.

Band, (GHz)	$T_{sys}$ , (K)
33 - 50 GHz	< 17 K
84 - 116 GHz	< 37 K
211 - 275 GHz	< 50 K
602 - 720 GHz	< 150 K

be obtained if spacecraft is in the line of sight from the center of ground based array and the target source. A proper signal processing and orbit parameter choice has an ability to provide reasonably convincing conclusions.

## 2 MILLIMETRON OBSERVATORY

Millimetron observatory will be a 10 meter deployable space telescope that is capable to operate at far infrared, sub-millimeter and millimeter space telescope (Kardashev et al. 2014). It will have two operating modes: single dish and Space-Earth VLBI. In order to achieve the best required sensitivity for the single-dish, the antenna and onboard instrumentation will be cooled down to 10 K and 4 K correspondingly.

Scientific tasks for the single-dish mode include the measurement of CMB spectral distortions and magnetic fields, observation of filamentary structure and search for the water trail in the Galaxy. Regarding the Space-Earth VLBI mode, Millimetron is aimed to study the vicinity of the nearest SMBHs (M87\* and Sgr A\*) with high angular resolution in a wide frequency range. The sensitivity of the observatory Millimetron will be orders of magnitude better than of Radioastron Kardashev et al. (2013). The design system temperature of VLBI receivers is shown in Table 1.

Millimetron space observatory will be operating in halo orbit around L2 point of the Sun-Earth system. It is a quasi-stable orbit located in the vicinity of L2 point in the plane perpendicular to the ecliptic plane. Such orbital configuration is the most suitable for single dish observations in terms of thermal and radiation conditions and it will provide the lowest possible temperature of the telescope mirror and thus allow to reach ultimate sensitivity.

The observatory will have an onboard memory, so that Space-Earth VLBI observations will be conducted without the simultaneous data transfer to the Earth. The signal will be in memory and transferred to the ground after the observation or in the gaps between.

## 3 SIMULATIONS

### 3.1 Setup

The main goal of presented simulations is to demonstrate the capabilities of Millimetron observatory Space-Earth VLBI imaging in L2 point orbit of averaged Sgr A\* and M87\*. In order to compare the results of L2 orbit imaging with HEO and ground only baseline the parameters of the simulations were taken the same as for Andrianov et al. (2021), including the configuration of ground array. Namely, bandwidth was set to  $\Delta\nu = 2$  GHz, total observing time  $t = 15$ , the observing frequency  $\nu = 230$  GHz and coherent integration time  $t_{int} \approx 10$  s.

All the calculations were performed using the Astro Space Locator Software (ASL) package for VLBI data processing and reduction (Likhachev et al. 2017; Zuga et al. 2017; Likhachev et al. 2020).

### 3.2 Source Models

In these simulations the models and scattering algorithms are the same as in Andrianov et al. (2021). In addition, we provide our own GRMHD models of M87\*. To create models, "harm2d" (Gammie et al. 2003; Noble et al. 2006) with a dimension of 2.5 D is used to obtain these models. An axisymmetric torus-like distribution of an ideal electron-proton plasma around a rotating black hole was considered. A black hole is described by the Kerr metric, which depends on two parameters: the mass and the spin of the black hole. The spin was set equal to  $a = 0.95$ . It is believed that the axis of rotation of the black hole is co-directed with the axis of rotation of the torus-like disk. The initial state is set as a Fishbone-Moncrief (Fishbone & Moncrief 1976) with the inner radius of the disk  $r_{in} = 6$  and the radius of maximum pressure  $r_{max} = 12$ . The relativistic equation of state of the disk with the adiabatic index equal to  $\Gamma = 4/3$  was used. The magnetic field is set in the form of a closed loop, the size and shape of which is set using a vector potential. The normalization of the vector potential is determined by the parameter  $\beta$  (see Gammie et al. (2003)), which is chosen to be equal to  $\beta = 100$ , that corresponds to the disk with standard and normal evolution (SANE-disk) (Chernov 2021). The numerical resolution of the grid is  $N_r \times N_\theta = 250 \times 250$  points.

The free code "grtrans" (Dexter 2016) is used to construct images of black holes. It is supposed that the observer is located at an angle  $i = 30^\circ$  to the axis of rotation of the black hole. It is assumed that relativistic electrons emit synchrotron radiation, taking into account absorption and Faraday effects (rotation and conversion). The distribution function of the emitting electrons was chosen to be equal to the relativistic thermal (Maxwell) distribution function with the electron temperature determined through the proton temperature. Three models (#1, #2 and #3 correspondingly) with the electron temperature equal to  $T_e = T_p/3$ ,  $T_e = T_p$ , and  $T_e = T_p/2$  are considered, where  $T_p$  - is the temperature of the proton. The mass of the black hole is given as  $M = 6.5 \times 10^9 M_\odot$ , where  $M_\odot$  is the mass of the Sun and the distance  $D = 16.4$  Mpc. For each model, the radiation flux is normalized at a frequency of  $\nu = 230$  GHz by an amount equal to  $J_{230} = 1$ ,  $J_{230} = 0.7$  and  $J_{230} = 0.8$  Jy accordingly that corresponds to the mass accretion rate of  $\dot{M} = 1.4 \times 10^{-4} \dot{M}_{edd}$ ,  $\dot{M} = 3.9 \times 10^{-4} \dot{M}_{edd}$  and  $\dot{M} = 8.7 \times 10^{-4} \dot{M}_{edd}$ , respectively, for the efficiency coefficient  $\eta = 0.057$  (Chael et al. 2017), where  $\dot{M}_{edd}$  - the Eddington mass accretion rate. Images of black holes are constructed at a frequency of  $\nu = 230$  GHz with a resolution of  $2500 \times 2500$  points. Each image has a distinct photon ring. A more detailed description of the models can be found in Chernov (2021).

### 3.3 Imaging Methodology

In presented simulations we use two methods of image deconvolution of the original models: CLEAN and maximum entropy method (MEM). Each of them has its own advantages and disadvantages, described in sufficient detail in the literature (see, for example, Thompson et al. (2017)). Since the black hole shadow model is, generally speaking, an extended source, MEM is the most appropriate deconvolution method. On the other hand, the model can contain small enough elements (for example, flares, bright compact spots, etc.) and for deconvolution of such image details CLEAN is a rather effective method.

Note that in comparison with linear reconstruction algorithms (CLEAN), the solutions obtained on the basis of the MEM (see D'Addario et al. (1973); Wernecke & D'Addario (1977)) provides higher quality restored images for extended and sources with com-

**Table 2.** Estimated phase noise for the EHT antennas at 230 GHz.

Telescope	$\Delta\phi_{rms}$ , deg/s
ALMA, Atacama, Chile	0.25
APEX, Atacama, Chile	0.25
GLT 12 m, Greenland	0.3
PV (IRAM 30 m), Pico Veleta, Spain	0.375
JCMT, Hawaii, USA	0.4
LMT 50 m, Mexico	0.45
SMT, Arizona, USA	0.35
SMA, Hawaii, USA	0.35
Kit Peak 10m, Arizona, USA	0.4
NOEMA, Plateau de Bure, France	0.45

plex structure. On the other hand, MEM requires a solution of nonlinear equations complex system. The target entropy functional is essentially nonlinear and can be used to extrapolate the values of the visibility function outside the bounded  $(u, v)$ -plane (the so-called "super-resolution").

In addition, as will be shown below, the use of both CLEAN and MEM deconvolution methods provide a reliable estimate of the quality of the reconstructed image (fidelity).

Image quality was estimated using standard image fidelity, SSIM and sharpness methods as presented in [Andrianov et al. \(2021\)](#). The sharpness of the inner edge is defined as the standard deviation of the difference between the reconstructed image and the model in the cross section along the right ascension axis.

### 3.4 Phase Errors

To evaluate the influence of phase errors on the quality of image reconstruction, phase noise was introduced into the simulated data of the M87\* source. The phase error  $\Delta\phi = \Delta\phi_0 + \Delta\phi_{rms}(t)$  was added to the phase of the model visibility function. Here,  $\Delta\phi_0$  is a random number from 0 to  $360^\circ$ , which corresponds to the uncertainty in the absolute initial phase value of a given antenna,  $\Delta\phi_{rms}(t)$  reflects the effect of the atmosphere phase noise on the phase of the visibility function. The phase noise of the atmosphere is modeled under the assumption of Gaussian random fluctuations with a root-mean-square deviation ([Thompson et al. 2017](#); [Event Horizon Telescope Collaboration et al. 2019b](#); [Holdaway & Helfer 1999](#)). The RMS phase values for the EHT antennas are shown in Table 2. The estimates were based on the average atmospheric characteristics at the EHT telescope sites ([Event Horizon Telescope Collaboration et al. 2019b,c](#)).

### 3.5 Orbital Configuration

To perform the simulations of S-E VLBI observations we have calculated an orbit around L2 point using the software for navigational and ballistic support developed in Astro Space Center. Orbit calculation method can be divided into following steps:

- Search for analytical halo orbit that meets the necessary requirements for baseline projections,  $(u, v)$  coverage and source visibility
- Check for stability of the orbit in the implemented force model
- Search for orbital regions that provide the best  $(u, v)$  coverage
- Integrate orbital region using an exact propagator
- Calculate  $(u, v)$  plane for a given orbital region

The force model accounts for such factors as the central gravitational field of the Earth, non-centrality of the Earth gravitational field

up to the 8th order (EGM96), as well as the attraction of the solar system bodies: the Moon, the Sun, Mercury, Venus, Mars, Jupiter, Saturn, Uranus, Neptune and Pluto. Additionally, the force model takes into account the contribution of the solar radiation pressure on the spacecraft.

The orbit is integrated using the Runge-Kutta method of 7(8)th order. The accuracy of this method is sufficient to predict the spacecraft orbit with an accuracy of  $\sim 5$  km over an interval of up to 100 days when the spacecraft moves at a characteristic speed of halo orbits ([Montenbruck 1992](#); [Schäfer 2002](#)). Such orbit integration accuracy is enough to conduct VLBI observations at the L2 point of the Sun-Earth system.

Fig. 1 shows the projections of calculated analytical halo orbit in the XY, XZ and YZ planes. The exit from the ecliptic plane in this orbit does not exceed 400 thousand km. The choice of such an exit from the ecliptic plane increases daily radio visibility of the spacecraft at the Russian tracking stations for regular communication and control sessions with the spacecraft.

Several regions were selected on the calculated orbit that provide acceptable  $(u, v)$  coverage for M87\* and Sgr A\* target sources (see Fig. 2). The  $(u, v)$  points of space-ground baselines cover the range of baseline projections from 0.8 to 3 Earth diameters for M87\* and from 1 to 3 Earth diameters for Sgr A\*. This makes it possible to perform the imaging of these sources with the resolution  $\sim 3$ -4 times higher than it was achieved by the EHT.

As it was previously mentioned, the Millimetron project is designed to operate in two modes: single-dish and VLBI mode. The single-dish mode requires the highest achievable levels of sensitivity. Thus the antenna and the scientific payload of Millimetron observatory will be mechanically cooled down to 10 K and 4 K correspondingly. In this case the orbit around the L2 point of the Sun-Earth system is optimal since the noise contribution from the Earth and the Moon is blocked by the spacecraft heat shields.

In order to fulfill all the scientific tasks in the VLBI mode it is necessary to have a halo orbit around the libration point of the Sun-Earth system such that would satisfy the necessary requirements for baseline projections and  $(u, v)$  coverage for the sources, listed as priority in Millimetron science case. Thus, the presented orbit can be optimized in the future to reduce the magnitude and number of corrections required to maintain the halo orbit as well as to increase the number of the sources for imaging. For example, Fig. 3 shows a halo orbit that is suitable for S-E VLBI observations with relatively short baseline projections  $< 5$  Earth diameters for the sources that are located close to the orbit tracks (blue lines in Fig. 3).

## 4 RESULTS

In our simulations we use one of the orbits located around L2 point that is capable of imaging observations of M87\* and Sgr A\* sources. We performed the corresponding simulations of S-E VLBI observations using several source models. The next step was to evaluate the quality of the obtained images and to compare the estimates to the results of ground-only VLBI and previously obtained values for highly elliptical near-Earth orbits (HEO).

To estimate the fidelity for M87\* as a reference we used images of model from Fig. 4 (a) and model which is Gaussian blurred with the expected beam size for the Millimetron+EHT combination shown as "Convolved". Result for M87\* are shown in Fig. 4 and 5 and the estimated image quality can be found in Tables 3 and 4. Simulated images for Sgr A\* are shown in Fig. 6 and corresponding image quality estimates are demonstrated in Table 6.

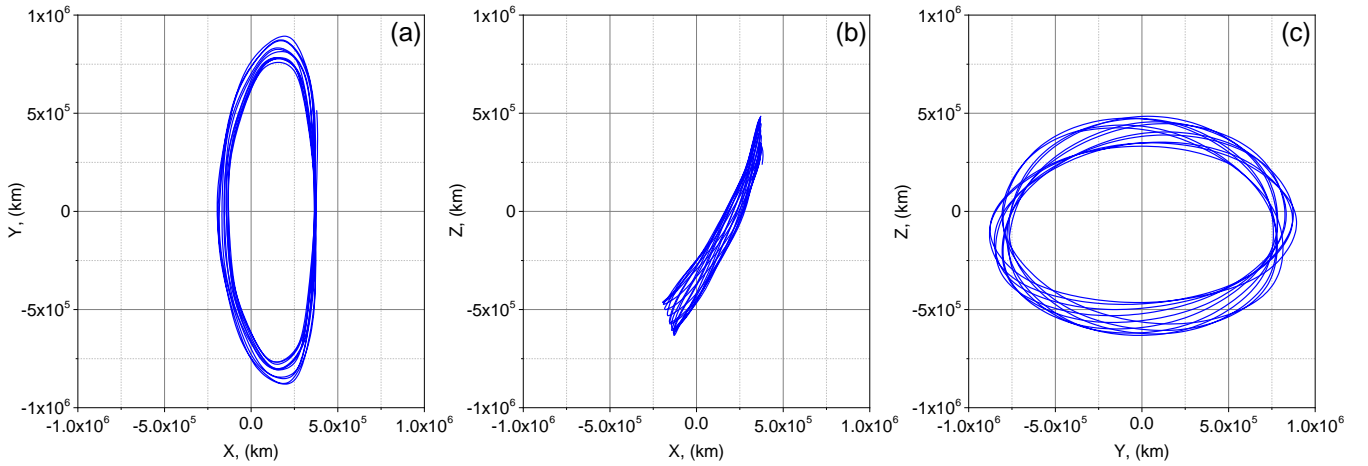


**Figure 1.** Projection of Millimetron L2 point halo orbit in L2 coordinate system (five orbital periods). (a) – XY-plane, (b) – XZ-plane, (c) – YZ-plane.

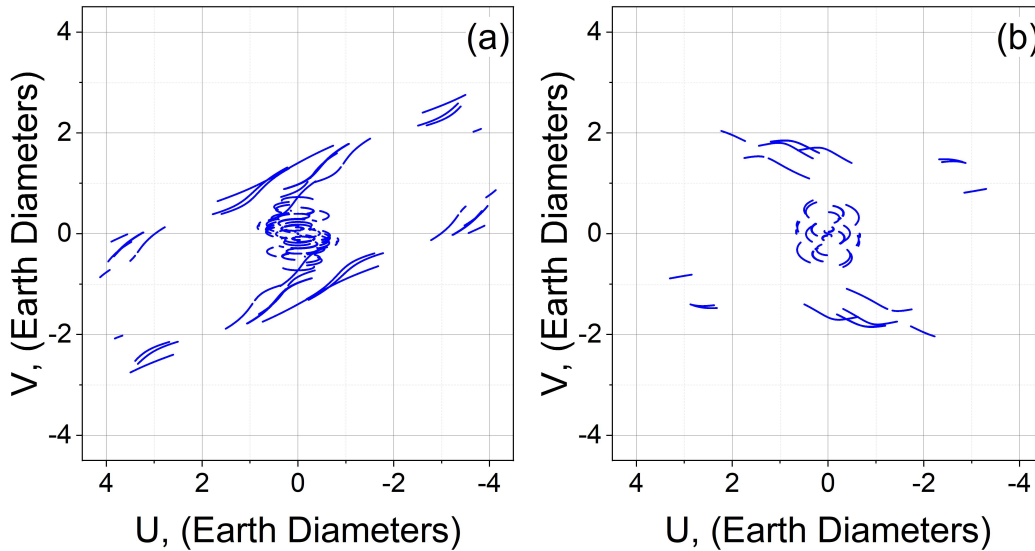


**Figure 2.**  $(u, v)$  coverage for M87\* (left) and Sgr A\* (right) for L2 point orbit of Millimetron+EHT configuration.

Comparing the M87\* image quality to the results obtained for highly elliptical near-Earth orbit, one can see from Table 5 that SSIM is 0.345 vs. 0.232 for HEO and L2 (model case) and 0.93 vs 0.948 for HEO and L2 (convolved model case); fidelity estimations are 12.56 vs 5.727 for HEO and L2 (model case) and 22.4 vs 18.482 for HEO and L2 (convolved model case).

The highest numbers both for fidelity and SSIM method are obtained for MEM image recovery technique both for EHT only and EHT+Millimetron observations. As expected EHT+Millimetron observations has superior image quality compared with EHT only. Though SSIM and fidelity for L2 orbit are slightly worse than those for HEO orbit, still these values are  $\sim 1.5 - 2$  times better than for ground only observations. The image quality figures obtained here for L2 orbit are very similar with figures obtained by analysis of the near-Earth elliptical orbit (Andrianov et al. 2021).

Speaking about the sharpness, its values are provided in Table 8. The lower the RMS value the better the sharpness. In order to avoid the effects of Doppler beaming at high inclination angles onto RMS,

the left part of models and obtained image profiles (see Table 8, last two columns) were analyzed separately. In most cases the EHT+MM synthetic observations show a better correspondence of sharpness comparing to the initial model. The exception is the model #16 of Sgr A\* where the absence of small-scale details in the model led to the RMS values that are close for both space-ground and ground only cases. In general, the sharpness for EHT+MM is  $\sim 1.5$  times better than for EHT only.

Finally, the resulting phase of the visibility model after applying phase errors to the M87\* data is shown in Fig. 7. Fig. 8 presents the result of M87\* image reconstruction after the global fringe fitting with phase closure. In the fringe fitting procedure the geometric disk was used as initial source model. As it can be seen from Fig. 6 (e) and Fig. 8 (c) the resulting images obtained without and with the phase noise after fringe fitting procedure are pretty much similar (see Table 7).

Considering the possibility of getting a better  $(u, v)$ -coverage, it should be noted that the selected halo-orbit around the point L2 is

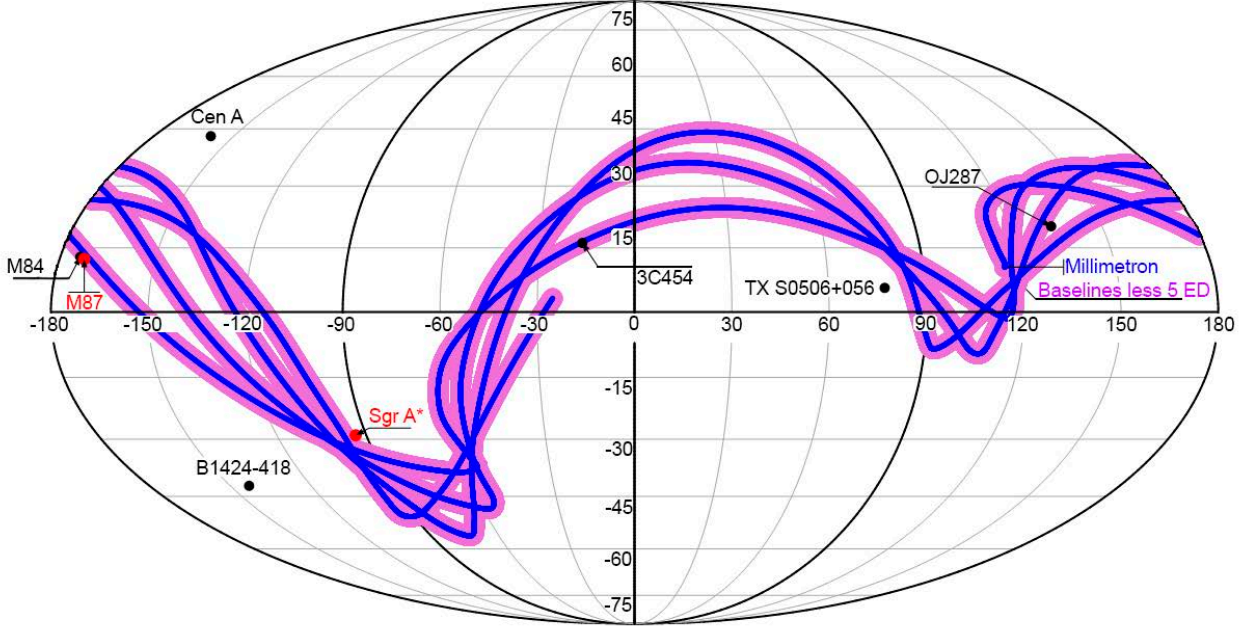


**Figure 3.** Mollweide projection of Millimetron orbit onto celestial sphere (blue lines) in the GCRF (Geocentric Celestial Reference Frame) for one of the orbits optimized for M87\* and Sgr A\* observations. Pink track on picture shows area of baseline projections less 5 Earth diameters.

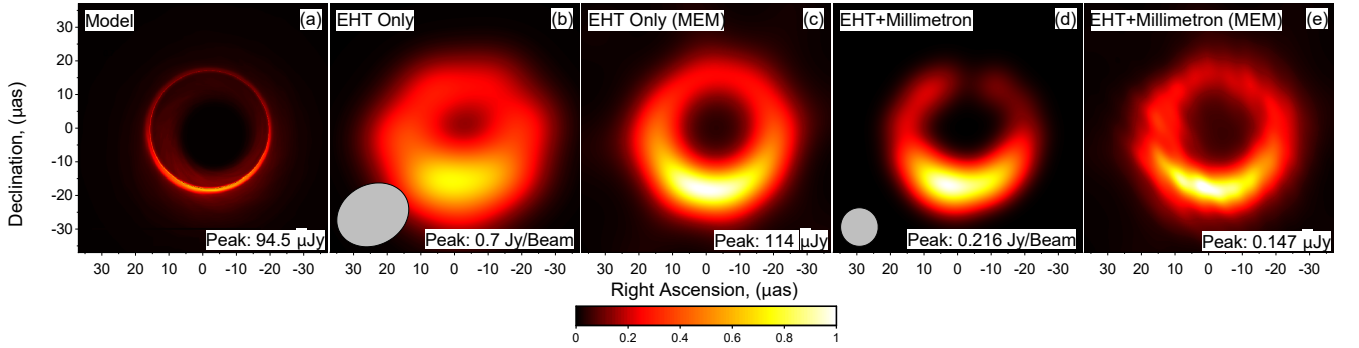


**Figure 4.** Simulated observations of M87\* for L2 point orbit (model by Johnson et al.): (a) – model, (b) and (c) – EHT only images obtained using CLEAN and MEM methods correspondingly, (d) and (e) – images obtained by Millimetron in L2 point orbit together with EHT using CLEAN and MEM methods correspondingly.

not unique and it belongs to the family of stable orbits, while the choice of a specific orbit from this family is dictated by the scientific program of the Millimetron project. Thus, the resulting orbit can be optimized to observe several sources at once with relatively short baseline projection and relatively good  $(u, v)$  coverage. Fig. 3 demonstrates that an orbit optimized for observations of only two sources (M87\* and Sgr A\*) is also capable of VLBI observations of sources close to the track lines at baseline projections less than 5 Earth diameters. Hence, more sources could be imaged.

## 5 CONCLUSIONS

The presented results of SMBH imaging using space-ground interferometer in L2 orbit show a significant improvement in the quality and resolution of the image relative to observations with ground-based only telescopes. The increase in angular resolution is about  $\sim 4$  times better, while the image fidelity, SSIM and sharpness values are  $\sim 2$  times better than those for ground-only observations and are comparable to those obtained for highly elliptical orbits in (Andrianov et al. 2021).

Thus, we conclude that the imaging capabilities of orbit located around the L2 Lagrange point of the Sun-Earth system are the same as for HEO. The results of fidelity and SSIM estimations prove that it

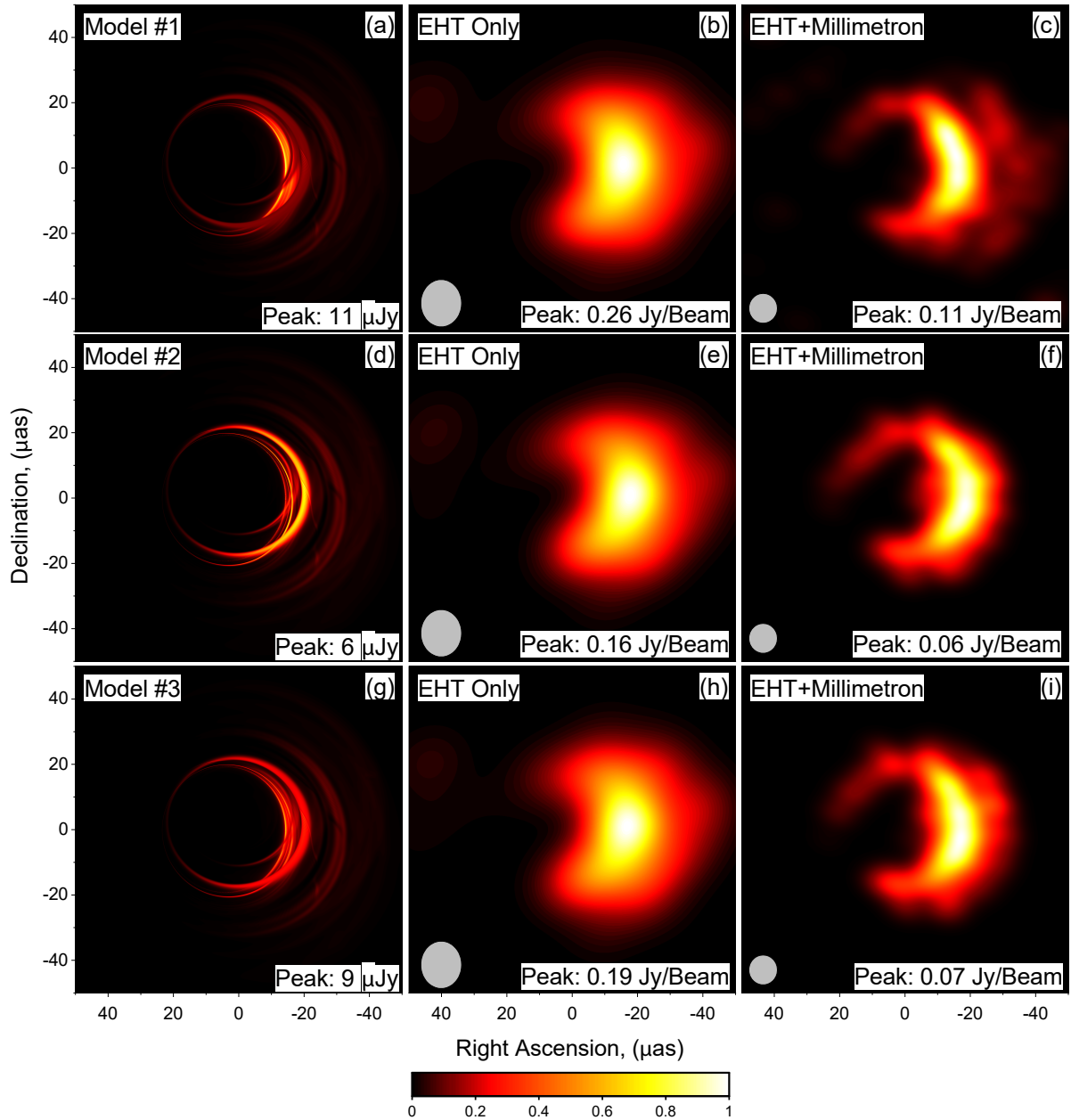


**Figure 5.** Simulated observations of M87\* for L2 point orbit (models by Chernov). Left column – models, middle column – EHT only images, right column – images obtained by Millimetron in L2 point orbit together with EHT.

is possible to obtain images of Sgr A\* and M87\* using an optimized orbit in Lagrange L2 point.

#### DATA AVAILABILITY

Data underlying related to the results of simulations in this article will be shared on reasonable request to the corresponding author.

#### ACKNOWLEDGEMENTS

The authors acknowledge Yuri Sheikinov for valuable comments. The authors acknowledge M. Mościbrodzka for providing the GRMHD models of Sgr A\* for the described simulations.

#### References

- Andrianov A. S., et al., 2021, *MNRAS*, **500**, 4866  
 Berti E., 2019, *General Relativity and Gravitation*, **51**, 140  
 Chael A. A., Narayan R., A. S., 2017, *MNRAS*, **470**, 2367  
 Chernov S. V., 2021, *Astronomy Reports*, **65**, 110  
 Cunha P. V. P., Herdeiro C. A. R., 2018, *General Relativity and Gravitation*, **50**, 42  
 D’Addario L. R., Wernecke S. J., Stark H., 1973, *IEEE Proceedings*, **61**, 671  
 Dexter J., 2016, *MNRAS*, **462**, 115  
 Event Horizon Telescope Collaboration et al., 2019a, *ApJ*, **875**, L1  
 Event Horizon Telescope Collaboration et al., 2019b, *ApJ*, **875**, L3  
 Event Horizon Telescope Collaboration et al., 2019c, *ApJ*, **875**, L4  
 Fishbone L. G., Moncrief V., 1976, *The Astrophysical Journal*, **207**, 962  
 Gammie G. F., McKinney J. C., Tóth G., 2003, *The Astrophysical Journal*, **589**, 444

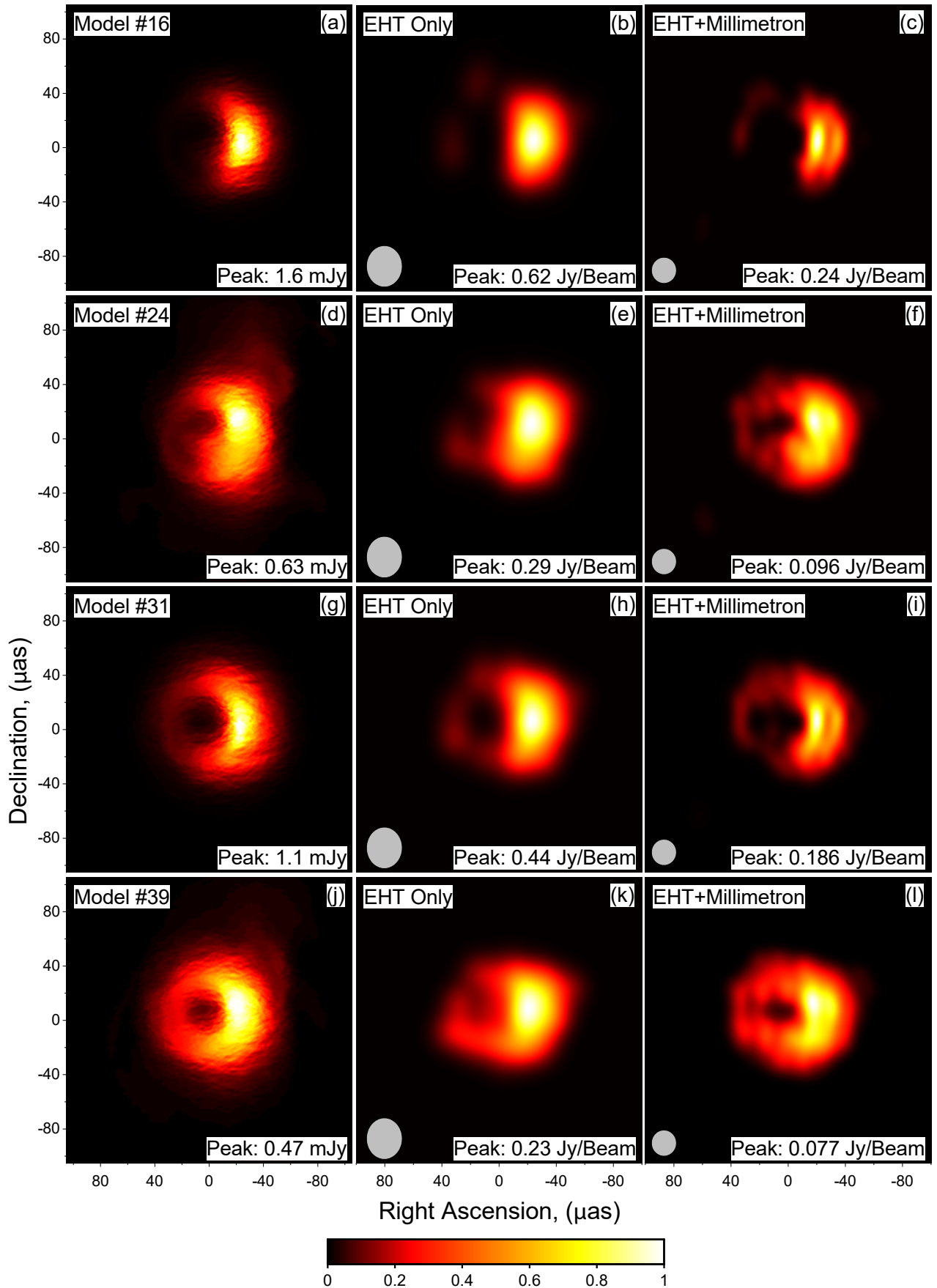


**Figure 6.** Simulated observations of Sgr A\* for L2 point orbit. Left column – models, middle column – EHT only images, right column – images obtained by Millimetron in L2 point orbit together with EHT.

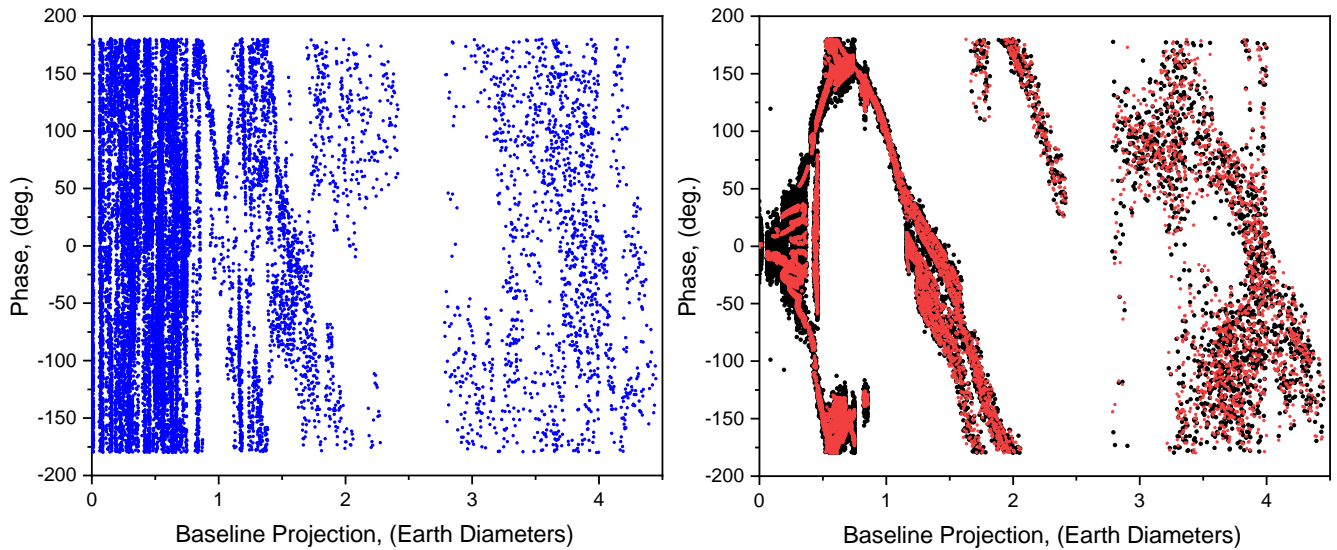


**Figure 7.** Phase vs. baseline projection for simulated observations of M87\*. Left panel shows introduced phase noise into data. Right panel corresponds to the resulting phase obtained from noisy data using fringe fitting procedure with M87\* model. Red dots on the right panel correspond to initial simulated phase without introducing the noise.

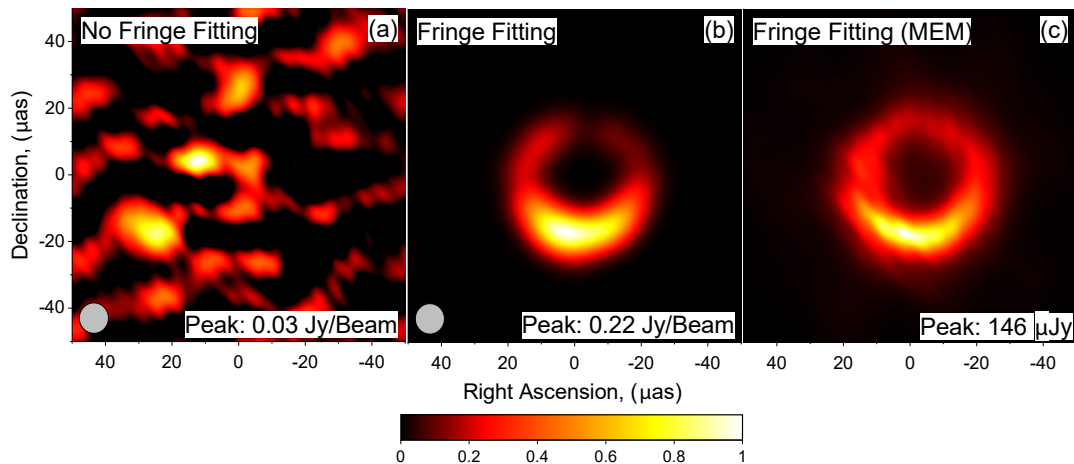


**Figure 8.** Reconstructed images of M87\* for phase noise case (model by Johnson et al.). Left panel shows the reconstructed image without fringe fitting, middle and right panels correspond to the reconstructed images after fringe fitting procedure using CLEAN and MEM methods correspondingly.

Holdaway M. A., Helfer T. T., 1999, in Taylor G. B., Carilli C. L., Perley R. A., eds, *Astronomical Society of the Pacific Conference Series* Vol. 180, *Synthesis Imaging in Radio Astronomy II*, p. 537  
 Kardashev N. S., et al., 2013, *Astronomy Reports*, **57**, 153  
 Kardashev N. S., et al., 2014, *Physics Uspekhi*, **57**, 1199  
 Likhachev S. F., Kostenko V. I., Girin I. A., Andrianov A. S., Rudnitskiy A. G., Zharov V. E., 2017, *Journal of Astronomical Instrumentation*, **6**, 1750004  
 Likhachev S., et al., 2020, *Astronomy and Computing*, **33**, 100426  
 Montenbruck O., 1992, *Celestial Mechanics and Dynamical Astronomy*, **53**, 59  
 Noble S. C., Gammie C. F., McKinney J. C., Del Zanna L., 2006, *The Astrophysical Journal*, **641**, 626  
 Novikov I. D., et al., 2021, *Physics-Uspekhi*, **64**, 386  
 Psaltis D., 2019, *General Relativity and Gravitation*, **51**, 137  
 Roelofs F., et al., 2019, *A&A*, **625**, A124

Schäfer W. A., 2002, in Warmbein B., ed., *ESA Special Publication* Vol. 500, *Asteroids, Comets, and Meteors: ACM 2002*, pp 345–349  
 Thompson A. R., Moran J. M., Swenson George W. J., 2017, *Interferometry and Synthesis in Radio Astronomy*, 3rd Edition. Springer, Cham, doi:<http://doi.org/10.1007/978-3-319-44431-4>  
 Wernecke S. J., D’Addario L. R., 1977, *IEEE Transactions on Communications*, **26**, 351  
 Zuga V. A., Rudnitskiy A. G., Likhachev S. F., 2017, *Bulletin of the Lebedev Physics Institute*, **44**, 21

This paper has been typeset from a  $\text{\TeX}/\text{\LaTeX}$  file prepared by the author.

**Table 3.** Fidelity and SSIM estimate for images obtained by CLEAN and MEM methods for M87\* simulations (Fig. 4).

CLEAN Method		Convolved	EHT	EHT+MM
SSIM	Model	0.187	0.064	0.232
	Convolved	1.000	0.702	0.948
Fidelity	Model	5.174	3.066	5.727
	Convolved	$\infty$	5.618	18.482
MEM Method		Convolved	EHT	EHT+MM
SSIM	Model	0.187	0.114	0.177
	Convolved	1.000	0.904	0.970
Fidelity	Model	5.174	3.986	5.232
	Convolved	$\infty$	12.011	21.278

**Table 4.** Fidelity and SSIM estimate for images obtained by CLEAN method for M87\* simulations (Fig. 5).

Model #1		Convolved	EHT	EHT+MM
SSIM	Model	0.160	0.074	0.162
	Convolved	1.000	0.833	0.948
Fidelity	Model	6.537	4.555	6.483
	Convolved	$\infty$	10.502	17.612
Model #2		Convolved	EHT	EHT+MM
SSIM	Model	0.248	0.128	0.223
	Convolved	1.000	0.847	0.908
Fidelity	Model	6.809	4.731	5.955
	Convolved	$\infty$	10.790	12.599
Model #3		Convolved	EHT	EHT+MM
SSIM	Model	0.233	0.106	0.308
	Convolved	1.000	0.816	0.851
Fidelity	Model	6.983	4.648	7.448
	Convolved	$\infty$	10.165	12.574

**Table 5.** Comparison of fidelity and SSIM for M87\* simulations with Millimetron on near-Earth orbit (Andrianov et al. 2021) and on halo-orbit.

		Near-Earth	Halo Orbit
SSIM	Model	0.345	0.232
	Convolved	0.930	0.948
Fidelity	Model	12.56	5.727
	Convolved	22.40	18.482

**Table 6.** Fidelity and SSIM estimate for images obtained by CLEAN methods for Sgr A\* simulations (Fig. 6).

Model #16		Convolved	EHT	EHT+MM
SSIM	Model	0.991	0.918	0.908
	Convolved	1.000	0.949	0.879
Fidelity	Model	69.521	22.392	26.964
	Convolved	$\infty$	26.901	24.443
Model #24		Convolved	EHT	EHT+MM
SSIM	Model	0.994	0.943	0.931
	Convolved	1.000	0.941	0.918
Fidelity	Model	64.518	18.735	20.619
	Convolved	$\infty$	19.407	19.607
Model #31		Convolved	EHT	EHT+MM
SSIM	Model	0.989	0.961	0.905
	Convolved	1.000	0.971	0.867
Fidelity	Model	52.949	23.248	22.026
	Convolved	$\infty$	27.011	19.123
Model #39		Convolved	EHT	EHT+MM
SSIM	Model	0.996	0.935	0.944
	Convolved	1.000	0.935	0.939
Fidelity	Model	59.396	17.429	21.127
	Convolved	$\infty$	18.214	20.960

**Table 7.** Fidelity and SSIM estimate compare for images of M87\* simulations obtained by MEM without phase errors (Fig. 4(c, e)) and with phase closure after adding errors (Fig. 8(c)).

With phase closure		Convolved	EHT	EHT+MM
SSIM	Model	0.187	0.114	0.177
	Convolved	1.000	0.904	0.970
Fidelity	Model	5.174	3.986	5.232
	Convolved	$\infty$	12.011	21.278
Without phase errors		Convolved	EHT	EHT+MM
SSIM	Model	0.187	0.114	0.176
	Convolved	1.000	0.905	0.970
Fidelity	Model	5.174	3.994	5.203
	Convolved	$\infty$	12.075	21.100

**Table 8.** Calculated sharpness for Sgr A\* and M87\*. The lower the value the better the sharpness.

#	EHT-Model	(EHT+MM)-Model	EHT-Model (left side only)	(EHT+MM)-Model (left side only)
Sgr A*				
16	0.0045	0.0049	0.0016	0.0016
24	0.0023	0.0018	0.0019	0.0015
31	0.0050	0.0037	0.0022	0.0018
39	0.0033	0.0025	0.0029	0.0029
M87*				
Johnson (Clean)	0.015	0.0091	0.01	0.001
Johnson (MEM)	0.0098	0.0073	0.0052	0.0038
Chernov #1	0.011	0.0074	0.0015	0.0003
Chernov #2	0.0098	0.007	0.001	0.0007
Chernov #3	0.0098	0.0061	0.0013	0.0003